Thank you for your valuable time in reviewing this manuscript. I hope you find the revised version satisfactory. However, if it still falls short, we would appreciate any additional suggestions you may have. Below, you will find our detailed point-by-point responses in blue.

Responses to the comment from Reviewer #1

Major comment:
This paper investigated the linear trend of oxygen concentration in the North Pacific and their relation to the circulation change. Deoxidization is an important issue not only for our scientific community but also for the broader society. Thus, many papers tackled in the issue (ex. Ito et al. 2017, 2024; Kolodziejczyk et al. 2024). However, in the manuscript, there is insufficient discussion to clarify the relationship with those previous studies. Furthermore, uncertainty is also inadequately discussed. Spatial distributions of uncertainty in mapped oxygen and that in linear regression are given, but there is no description how these uncertainties affect the results. Since oxygen concentration in GOBAI-O2 are estimated by using temperature and salinity information, uncertainties need to be fully investigated before discussing physical implications.

>there is insufficient discussion to clarify the relationship with those previous studies. Furthermore, uncertainty is also inadequately discussed.

We checked the relevant papers (Ito et al. 2017, 2024; Kolodziejczyk et al. 2024) and compared our results with them, especially Ito et al. (2017). It is because Ito et al. (2017) showed the linear trends in dissolved O_2. As for Kolodziejczyk et al. (2024), they used the ISASO2 ARGO fields with the World Ocean Atlas, but their data have many gaps in the north Pacific, which makes it relatively difficult to compare with the linear trends in the current study.

The revised parts in Section 3.2 can read:

"Compared with the historical horizontal distributions of dissolved O_2 in the North Pacific reported by Ito et al. [2017] (Figure 3 in Ito et al. 2017), our negative trend extends over a broader area. The positive trend detected in the Kuroshio-Oyashio Transition Zone and the northeastern region, with a density range of 26.8–27.0σ_θ (Figure 1r), was not evident in the distribution presented by Ito et al. [2017]. Similarly, the positive trend observed in the tropical western Pacific below 400 m depth (Figure 1r–t) is relatively stronger than

that identified in their analysis (Figure 3 in Ito et al. [2017]). The positive trend in dissolved O_2 in the Kuroshio–Oyashio Transition Zone coincides with a region of low uncertainty values (Fig. 1p–s and 1w–y), suggesting this signal may result from the high observation frequency by Argo profiling floats. Other regions exhibiting positive signals—the northeastern region with a density range of 26.8–27.0σ_θ (170°E–150°W, 45–55°N, Fig. 1r) and the tropical western Pacific (130°–170°E, 0°–10°N, Figure 1r–t)—also correspond to areas of low uncertainty (Fig. 1y-aa). Therefore, these pronounced positive trends likely represent highly reliable increases in dissolved O_2, implying a robust deoxygenation signal."

>Spatial distributions of uncertainty in mapped oxygen and that in linear regression are given, but there is no description how these uncertainties affect the results. Since oxygen concentration in GOBAI-O2 are estimated by using temperature and salinity information, uncertainties need to be fully investigated before discussing physical implications.

Regarding uncertainty, another reviewer also pointed this out. We therefore have added figures illustrating uncertainty (Figures 1-4, Supplementary Figures S1-S4) and supplemented the description concerning uncertainty.

In Sharp et al. (2023), the uncertainty was evaluated by three uncertainty components (see below). The GOBAI-O_2 dataset provides uncertainty data alongside potential temperature, salinity, and dissolved oxygen. In section 2 of the revised manuscript, we added the sentences how uncertainty was estimated in Sharp et al. (2023). Furthermore, we added a figure next to the one showing the linear trend for oxygen, using the same format and displaying the average uncertainty for all sites during the target period (Figures 1-4, Supplementary Figures S1-4). This revision allowed readers to understand the magnitude of uncertainty at sites showing a linear trend for oxygen.

The relevant parts are addressed now in Section 2:
"The uncertainty of GOBAI-O_2 datasets [Sharp et al., 2023] is estimated by uncertainty estimates, in which the individual uncertainty components are combined in quadrature (assuming independence) to assess the uncertainty of dissolved O_2 data for each gridded $[O_2]$ value:

$$u([O_2])_{tot.} = \sqrt{u([O_2])^2{}_{meas.} + u([O_2])^2{}_{grid.} + u([O_2])^2{}_{alg.}} \qquad (1),$$

where $u([O_2])^2{}_{meas.}$ represents the measurement uncertainty of the $[O_2]$ observation themselves, $u([O_2])^2{}_{grid.}$) reflects the gridding uncertainty arising from a single $[O_2]$ value to represent a four-dimensional box that is coarser in time and space than the resolution of many processes influencing $[O_2]$, and $u([O_2])^2{}_{alg.}$ corresponds to the algorithmic uncertainty from the machine-learning methods used to estimate $[O_2]$ on the grid of Roemmich and Gilson (2009) data. We use this uncertainty estimate $u([O_2])_{tot.}$ and evaluate their uncertainty for estimating oxygen trends (Figs. 1–4). The mean uncertainty is added when calculating the linear trend in oxygen for almost all figures in this study."

The relevant parts are addressed now in Section 3.1:
"The total uncertainty in dissolved O_2, $u([O_2])_{tot.}$, in these layers (Fig. 1v–bb) indicates that large values exist in the northern Pacific above 50°N and gradually become smaller to the south. The relatively large uncertainty values are shown in the surface layer, and the steeper gradients of density in the tropical eastern region [150°–120°W, 10–30°N] at 100–200m depth (Fig. 1w–x). These large uncertainties typically exhibit a maximum of 100 m and tend to decrease with depth (Fig. 2 and Figure A14 in Sharp et al. [2023]). Regionally large uncertainty has been shown to depend primarily on algorithmic uncertainty in Figure 8 in Sharp et al. [2023] among the three components (measurement uncertainty, gridding uncertainty, and algorithm uncertainty) contributing to the total uncertainty (Eq. 1). Algorithmic uncertainty generally decreases with increasing spatio-temporal coverage of the available training data. The fact that greater regional algorithmic uncertainty is observed in the northern Pacific above 50°N and in the western and eastern Pacific coastal regions below 20°N suggests that the sampling data are sparse in those areas, and actually, their data sampling is low (Figure 1 in Sharp et al. 2023)."

"Some artificially induced or unnatural expansions of the trend are also observed (e.g. 170–130°W, 0–20°N), particularly in dissolved O_2 (Fig. 1q–s; Fig. 4i). The uncertainty estimates (Fig. 1v-bb) clearly indicate certain locations and depths with large values, sometimes exceeding 15 μmol/kg. Uncertainties are generally within 10 μmol/kg in the North Pacific. Such large uncertainties arise from limited observational data and high background variability [Sharp et al. 2023]. Areas with strong variability and steep background O_2 gradients tend to exhibit larger uncertainties than the global mean. An additional potential source of errors is a bias in sensor calibration for Argo-O_2 observations, which may arise from the finite response time of optode sensors and can

cause systematic bias in the oxycline regions [Bittig et al., 2014; 2018a,b]. Despite these uncertainties, our analysis shows that the observed trends are spatially coherent and connected smoothly each other, and then we can relate them to well-known physical mechanisms in the North Pacific. The GOBAI-O_2 dataset is, therefore, expected to provide improved insights into other oceanic biogeochemical processes and physical phenomena from an aerial perspective."

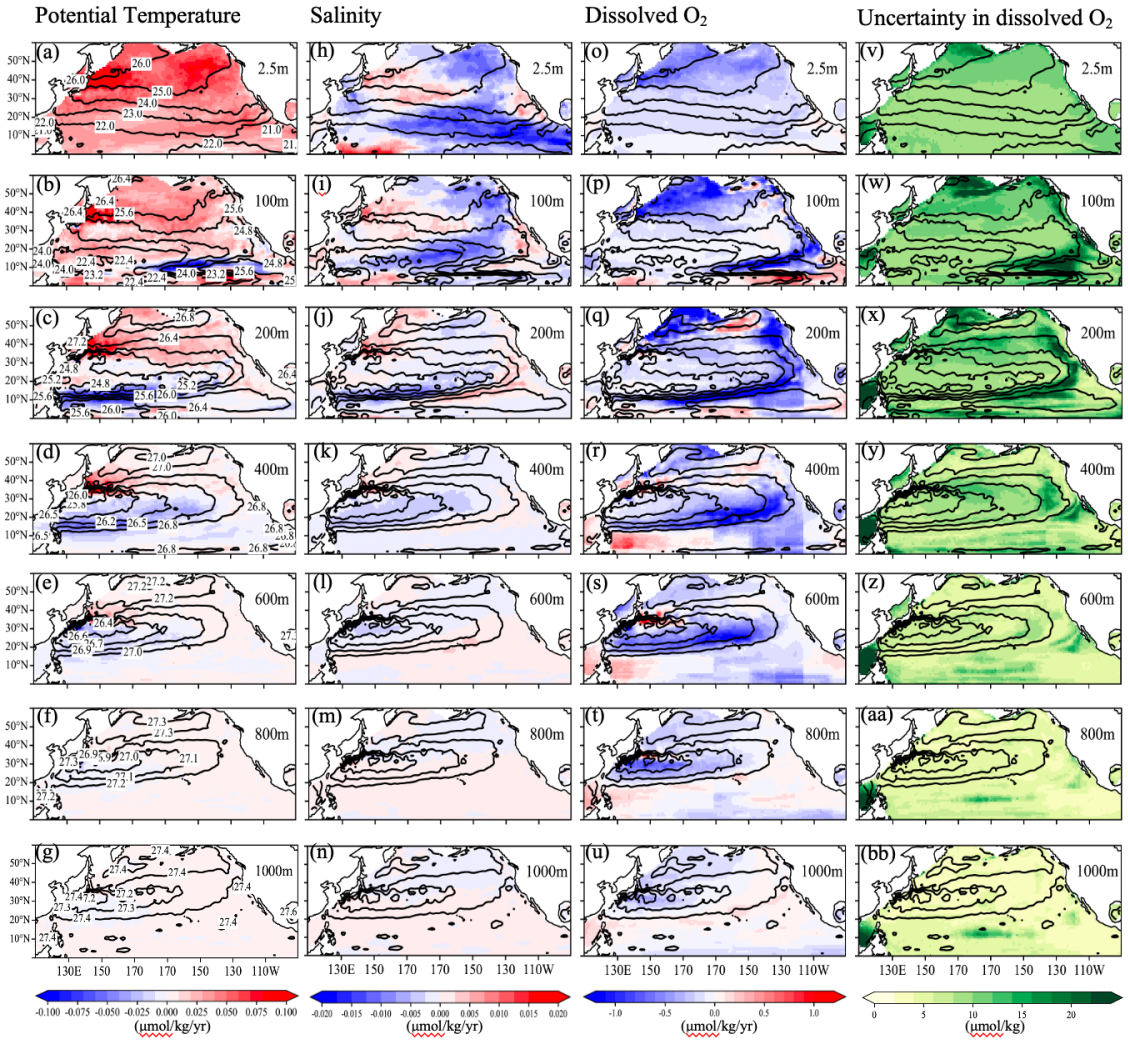

Figure 1 in the revised manuscript: Horizontal distributions of linear trends (μmol/kg/yr) in (a–g) potential temperature, (h–n) salinity, and (o–u) dissolved oxygen (O_2) during the observational period at depths of 0, 100, 200, 400, 600, 800, and 1000 m, respectively. Contours denote potential density at each depth. Labels for the potential density are shown only in the potential temperature sections. Corresponding distributions of the mean uncertainty in dissolved O_2 (μmol/kg) are presented in panels (v–bb).

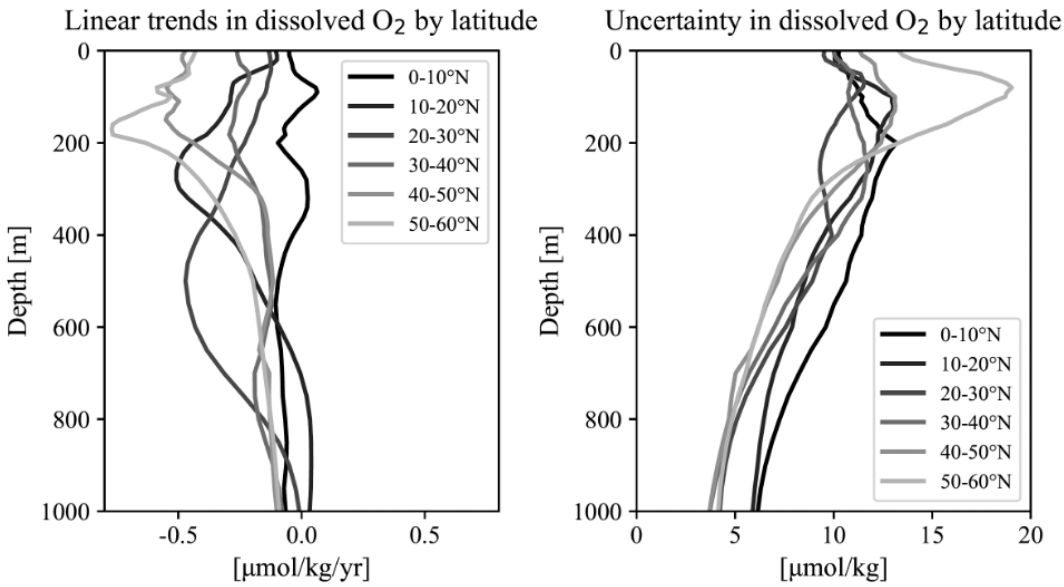

Figure 2 in the revised manuscript: Vertical profiles of linear trends and uncertainty in dissolved O_2 by latitude.

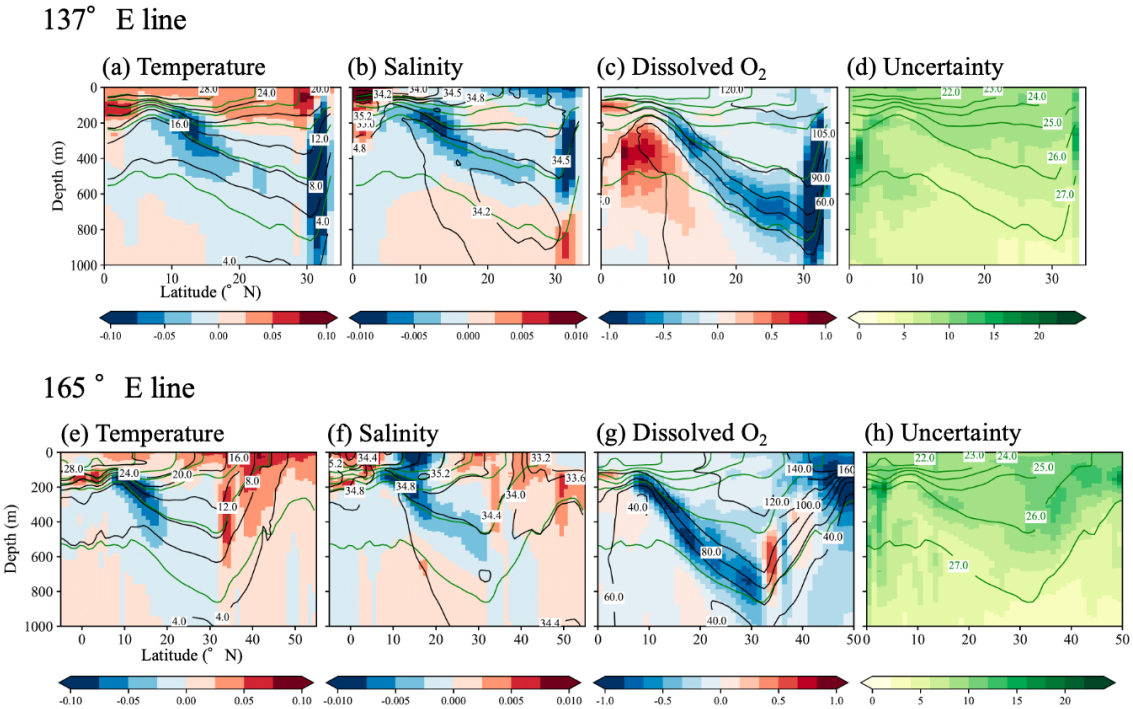

Figure 3 in the revised manuscript: Vertical sections showing linear trends in potential temperature (a, e), salinity (b, f), and dissolved O_2 (c, g) along the 137°E and 165°E meridians, respectively. Corresponding vertical sections of the mean uncertainty are presented in panels (d) and (h). Black contour lines indicate the mean potential

temperature (a, e), salinity (b, f), and dissolved oxygen (c, g) over the period 2004–2023, while green contour lines represent the mean potential density. Labels for the potential density are shown only in the uncertainty sections.

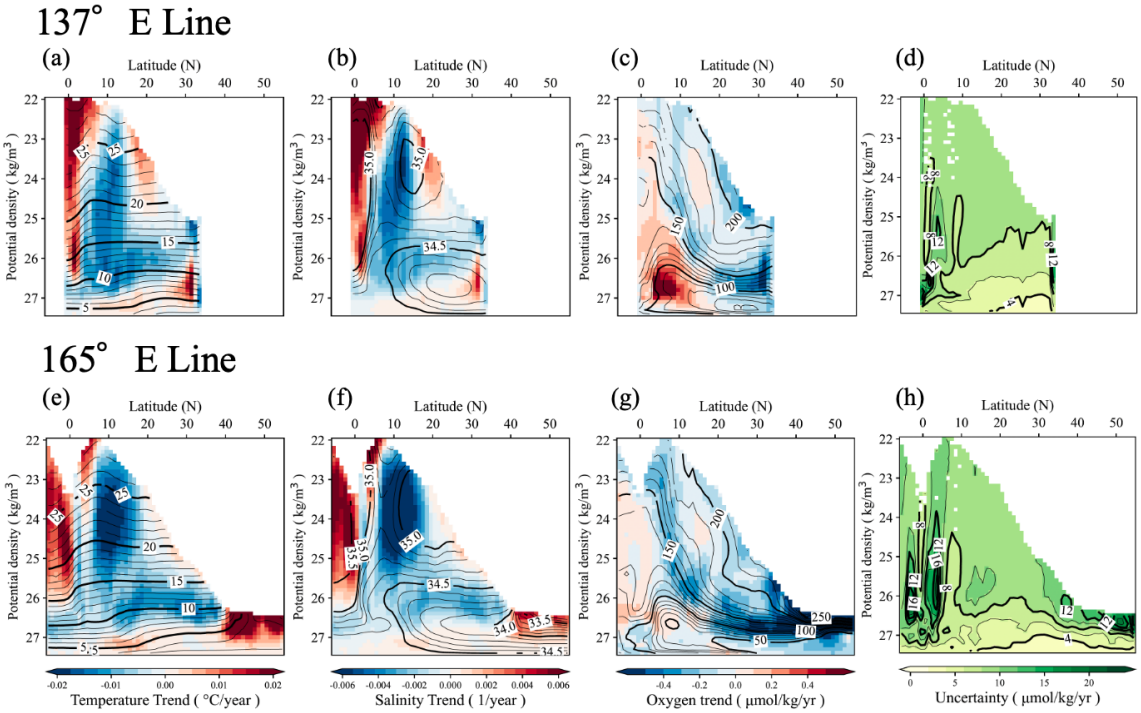

Figure 4 in the revised manuscript: Linear trends in (a, e) potential temperature, (b, f) salinity, (c, g), and dissolved O_2 on each isopycnal surface at intervals of $0.1\sigma_\theta$, calculated at every 1.0 deg of latitude in 137 °E and 165 °E lines, respectively. Contour lines represent the mean values during the target observation periods, plotted at intervals of $0.1\sigma_\theta$ for each 1 deg. of latitude. Fig. 4(d) and 4(h) are the same but show the averaged uncertainty during the target observation periods, on each isopycnal surface.

Minor comment:

Line 364, "areal areas"?

This part was deleted in the revised manuscript.

Responses to the comment from Reviewer #2

The manuscript examines two decades of linear trends in temperature, salinity, and dissolved oxygen in the North Pacific using the GOBAI-O2 dataset. This timely topic addresses the significant issue of ocean deoxygenation, and the emergence of biogeochemical Argo products offers new avenues for basin-scale analysis. The results align with previous ship-based observations, while also highlighting spatial heterogeneity in oxygen trends attributed to circulation changes like the retreat of the oxygen minimum layer and the northward migration of the subtropical–subarctic front.

The study is potentially valuable, but the manuscript in its present form does not sufficiently establish what is new compared to earlier syntheses. The discussion of previous work, notably Ito et al. (2017, 2024), Sasano et al. (2014), and Kolodziejczyk et al. (2024), is too brief. The paper sometimes reads as a confirmation exercise, whereas it should highlight more clearly what GOBAI-O2 reveals that was inaccessible with earlier datasets.

Reviewer #1 similarly noted insufficient comparison with prior studies. We therefore reviewed relevant papers (Ito et al. 2017, 2024; Kolodziejczyk et al. 2024) and added a comparison specifically with Ito et al. (2017), because Ito et al. (2017) similarly showed a linear trend for O_2. Kolodziejczyk et al. (2024) used the ISASO2 ARGO field from the World Ocean Atlas, but their dataset has numerous data gaps in the North Pacific, making comparison with the linear trend in this study relatively difficult. Therefore, we were unable to perform a comparison.

The revised parts in Section 3.2 can read:

"Compared with the historical horizontal distributions of dissolved O_2 in the North Pacific reported by Ito et al. [2017] (Figure 3 in Ito et al. 2017), our negative trend extends over a broader area. The positive trend detected in the Kuroshio-Oyashio Transition Zone and the northeastern region, with a density range of 26.8–27.0σ_θ (Figure 1r), was not evident in the distribution presented by Ito et al. [2017]. Similarly, the positive trend observed in the tropical western Pacific below 400 m depth (Figure 1r–t) is relatively stronger than that identified in their analysis (Figure 3 in Ito et al. [2017]). The positive trend in dissolved O_2 in the Kuroshio–Oyashio Transition Zone coincides with a region of low uncertainty values (Fig. 1p–s and 1w–y), suggesting this signal may result from the high observation frequency by Argo profiling floats. Other regions exhibiting positive

signals—the northeastern region with a density range of 26.8–27.0σ_θ (170°E–150°W, 45–55°N, Fig. 1r) and the tropical western Pacific (130°–170°E, 0°–10°N, Figure 1r–t)—also correspond to areas of low uncertainty (Fig. 1y-aa). Therefore, these pronounced positive trends likely represent highly reliable increases in dissolved O_2, implying a robust deoxygenation signal."

A more serious concern is the treatment of uncertainty. While fields of uncertainty are presented, their implications for the robustness of the detected trends are not discussed. In several regions the uncertainty is of the same order as the trends themselves. Furthermore, recent work has identified a systematic negative bias in oxygen from air-calibrated BGC-Argo floats relative to shipboard reference profiles, with offsets of roughly –2.7 µmol kg-1 at depth, which propagate into carbonate system estimates such as pCO2 (+3.2 µatm; Bushinsky et al., 2025). Since GOBAI-O2 is trained on these float observations, such biases must be considered explicitly. Without a careful discussion of these uncertainties, the attribution of observed patterns to physical processes remains premature.

The relevant parts are addressed now in Section 2:
"The uncertainty of GOBAI-O_2 datasets [Sharp et al., 2023] is estimated by uncertainty estimates, in which the individual uncertainty components are combined in quadrature (assuming independence) to assess the uncertainty of dissolved O_2 data for each gridded [O_2] value:

$$u([O_2])_{tot.} = \sqrt{u([O_2])^2{}_{meas.} + u([O_2])^2{}_{grid.} + u([O_2])^2{}_{alg.}} \qquad (1),$$

where $u([O_2])^2{}_{meas.}$ represents the measurement uncertainty of the $[O_2]$ observation themselves, $u([O_2])^2{}_{grid.}$) reflects the gridding uncertainty arising from a single $[O_2]$ value to represent a four-dimensional box that is coarser in time and space than the resolution of many processes influencing $[O_2]$, and $u([O_2])^2{}_{alg.}$ corresponds to the algorithmic uncertainty from the machine-learning methods used to estimate $[O_2]$ on the grid of Roemmich and Gilson (2009) data. We use this uncertainty estimate $u([O_2])_{tot.}$ and evaluate their uncertainty for estimating oxygen trends (Figs. 1–4). The mean uncertainty is added when calculating the linear trend in oxygen for almost all figures in this study."

The relevant parts are addressed now in Section 3.1:

"The total uncertainty in dissolved O_2, $u([O_2])_{tot.}$, in these layers (Fig. 1v–bb) indicates that large values exist in the northern Pacific above 50°N and gradually become smaller to the south. The relatively large uncertainty values are shown in the surface layer, and the steeper gradients of density in the tropical eastern region [150°–120°W, 10–30°N] at 100–200m depth (Fig. 1w–x). These large uncertainties typically exhibit a maximum of 100 m and tend to decrease with depth (Fig. 2 and Figure A14 in Sharp et al. [2023]). Regionally large uncertainty has been shown to depend primarily on algorithmic uncertainty in Figure 8 in Sharp et al. [2023] among the three components (measurement uncertainty, gridding uncertainty, and algorithm uncertainty) contributing to the total uncertainty (Eq. 1). Algorithmic uncertainty generally decreases with increasing spatio-temporal coverage of the available training data. The fact that greater regional algorithmic uncertainty is observed in the northern Pacific above 50°N and in the western and eastern Pacific coastal regions below 20°N suggests that the sampling data are sparse in those areas, and actually, their data sampling is low (Figure 1 in Sharp et al. 2023)."

"Some artificially induced or unnatural expansions of the trend are also observed (e.g. 170–130°W, 0–20°N), particularly in dissolved O_2 (Fig. 1q–s; Fig. 4i). The uncertainty estimates (Fig. 1v-bb) clearly indicate certain locations and depths with large values, sometimes exceeding 15 μmol/kg. Uncertainties are generally within 10 μmol/kg in the North Pacific. Such large uncertainties arise from limited observational data and high background variability [Sharp et al. 2023]. Areas with strong variability and steep background O_2 gradients tend to exhibit larger uncertainties than the global mean. An additional potential source of errors is a bias in sensor calibration for Argo-O_2 observations, which may arise from the finite response time of optode sensors and can cause systematic bias in the oxycline regions [Bittig et al., 2014; 2018a,b]. Despite these uncertainties, our analysis shows that the observed trends are spatially coherent and connected smoothly each other, and then we can relate them to well-known physical mechanisms in the North Pacific. The GOBAI-O_2 dataset is, therefore, expected to provide improved insights into other oceanic biogeochemical processes and physical phenomena from an aerial perspective."

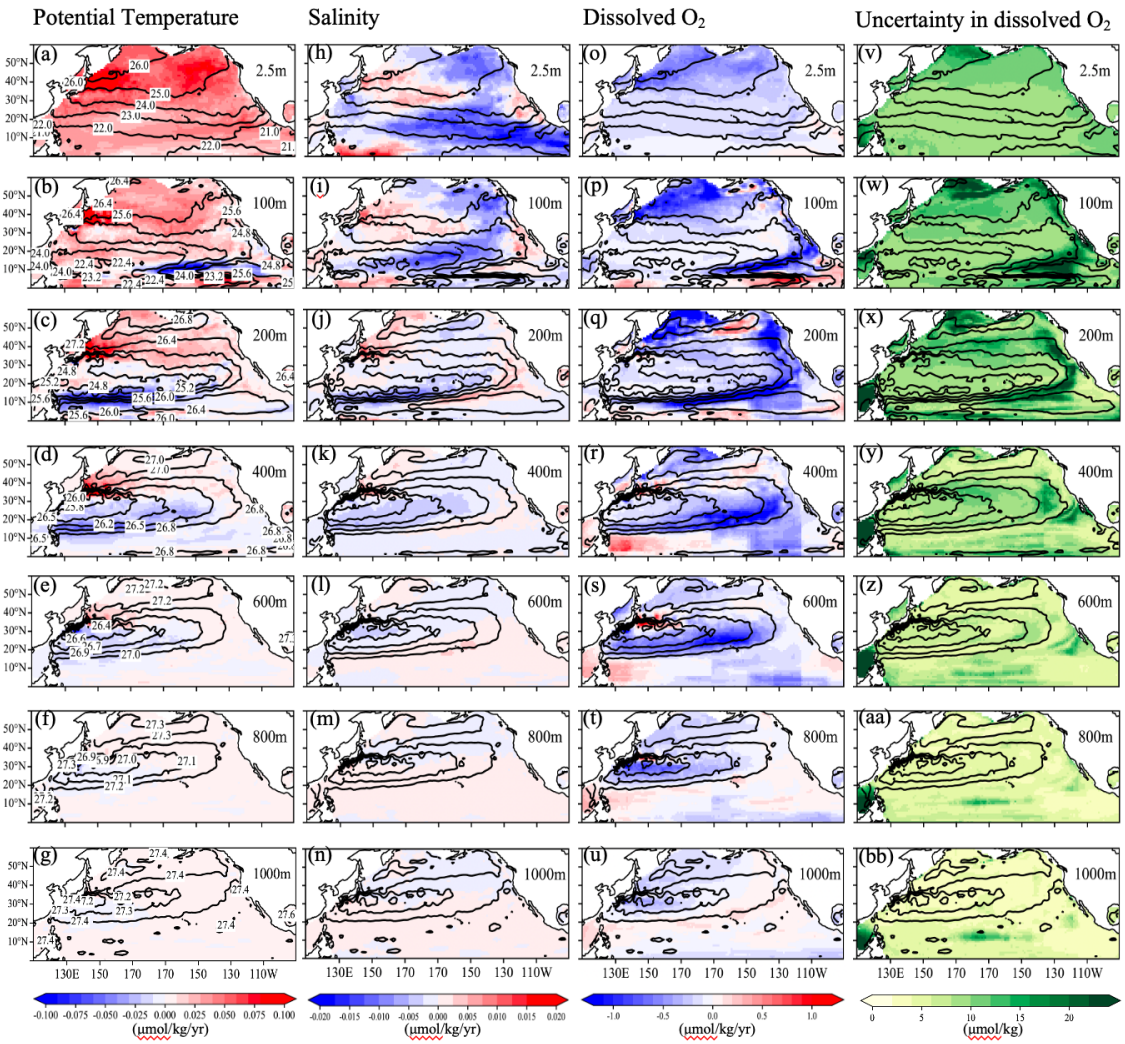

Figure 1 in the revised manuscript: Horizontal distributions of linear trends (μmol/kg/yr) in (a–g) potential temperature, (h–n) salinity, and (o–u) dissolved oxygen (O_2) during the observational period at depths of 0, 100, 200, 400, 600, 800, and 1000 m, respectively. Contours denote potential density at each depth. Labels for the potential density are shown only in the potential temperature sections. Corresponding distributions of the mean uncertainty in dissolved O_2 (μmol/kg) are presented in panels (v–bb).

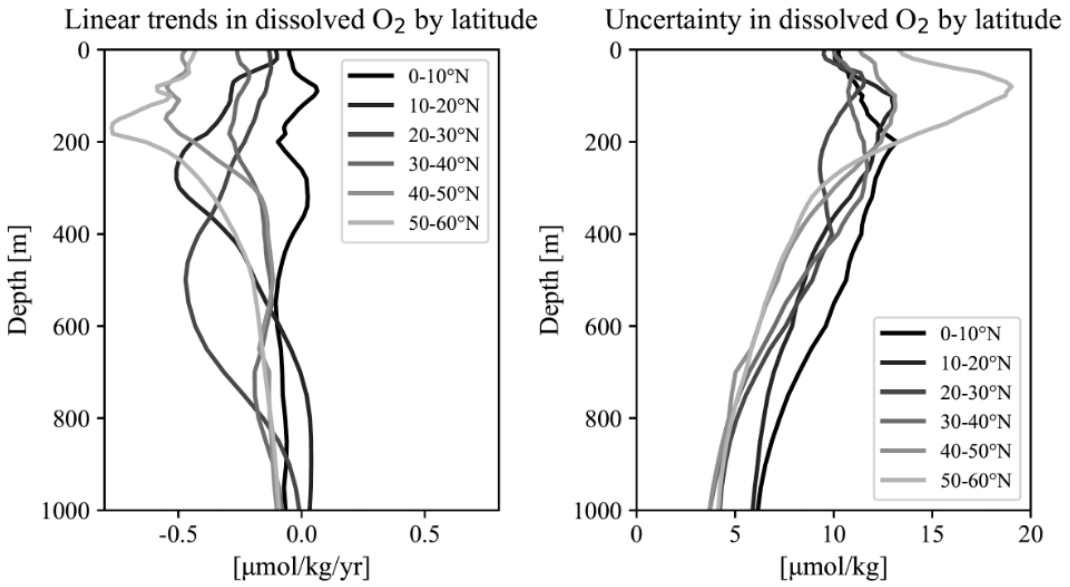

Figure 2 in the revised manuscript: Vertical profiles of linear trends and uncertainty in dissolved O_2 by latitude.

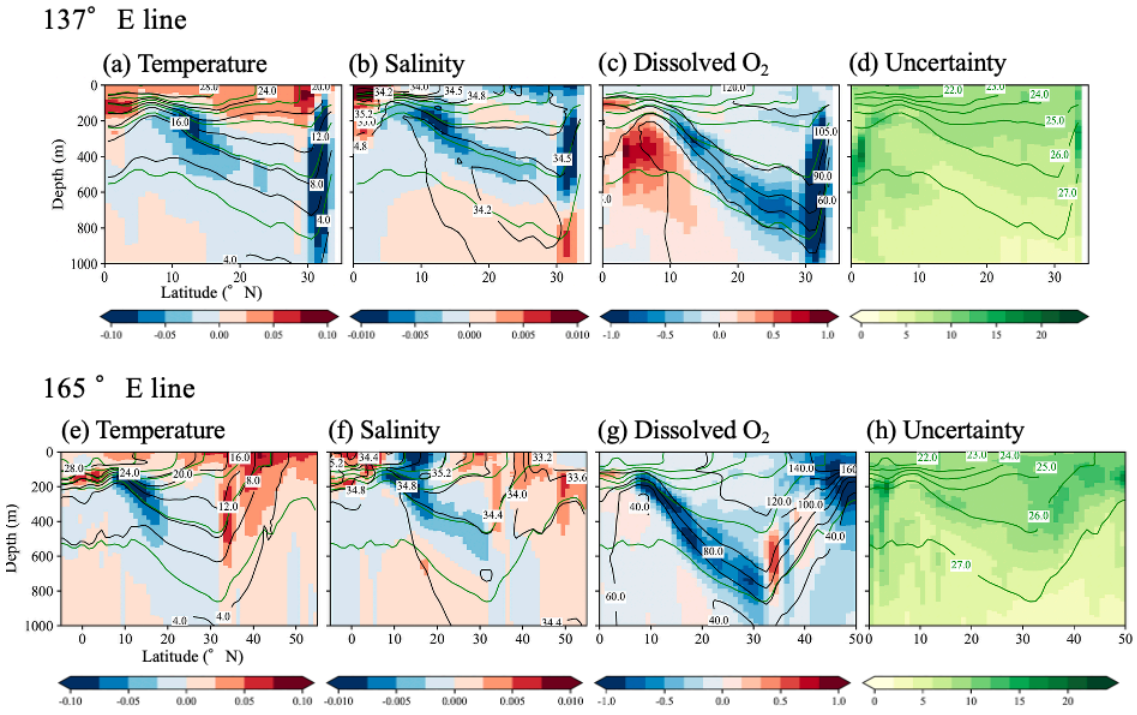

Figure 3 in the revised manuscript: Vertical sections showing linear trends in potential temperature (a, e), salinity (b, f), and dissolved O_2 (c, g) along the 137°E and 165°E meridians, respectively. Corresponding vertical sections of the mean uncertainty are presented in panels (d) and (h). Black contour lines indicate the mean potential

temperature (a, e), salinity (b, f), and dissolved oxygen (c, g) over the period 2004–2023, while green contour lines represent the mean potential density. Labels for the potential density are shown only in the uncertainty sections.

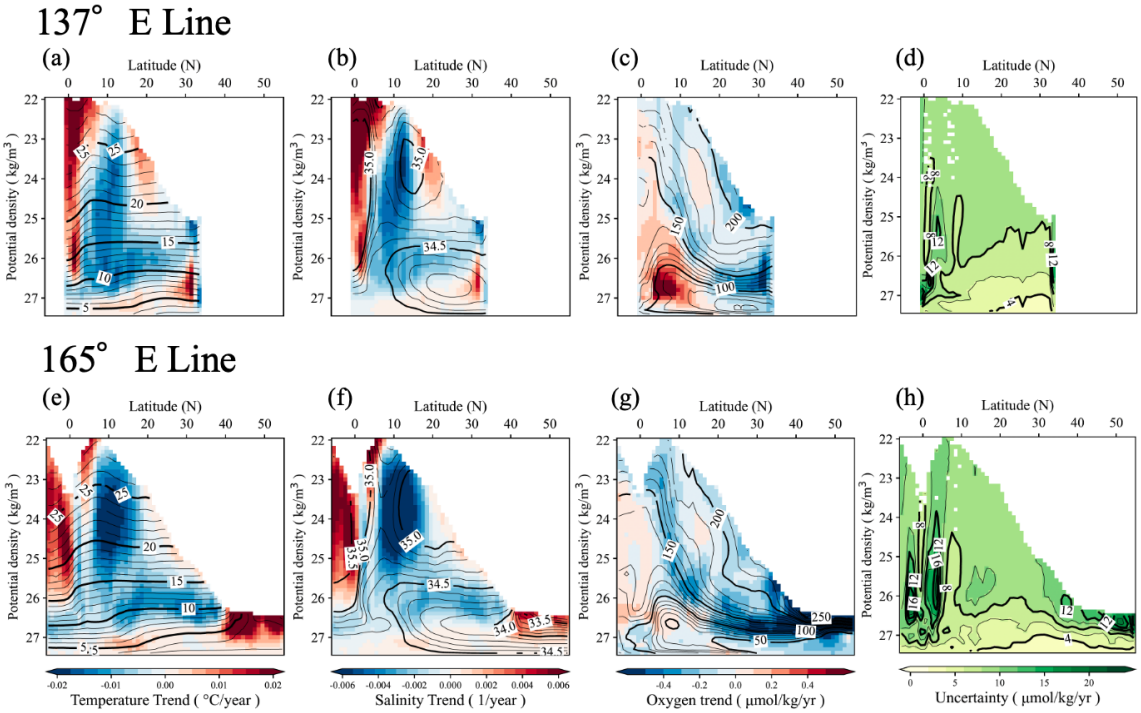

Figure 4 in the revised manuscript: Linear trends in (a, e) potential temperature, (b, f) salinity, (c, g), and dissolved O_2 on each isopycnal surface at intervals of $0.1\sigma_\theta$, calculated at every 1.0 deg of latitude in 137 °E and 165 °E lines, respectively. Contour lines represent the mean values during the target observation periods, plotted at intervals of $0.1\sigma_\theta$ for each 1 deg. of latitude. Fig. 4(d) and 4(h) are the same but show the averaged uncertainty during the target observation periods, on each isopycnal surface.

On the methodological side, the decision to interpolate GOBAI-O2 fields to 1 m vertical resolution requires justification, as it may artificially smooth variability.

Thank you for the comment. We interpolated the GOBAI-O_2 fields onto a 1-m vertical grid to ensure consistency in our diagnostics and to better resolve near-surface gradients. To evaluate whether this procedure introduces any artificial smoothing, we conducted sensitivity tests using multiple interpolation methods—linear, shape-preserving cubic (PCHIP), and cubic spline interpolation—and several target vertical resolutions (1m, 2m, and 5m) for Figure 4. The results (Figures S1 and S2) show no clear differences among the three interpolation methods (Figures S1a,b and S2a,b). Regarding the effects of

vertical resolution, a 5-m grid fails to resolve densities lighter than 24.0σ_θ at some latitudes (Figure S1d, S2d), but the main features of the fields are preserved across all tested resolutions. We have added a brief description of these tests and their results to Supplementary Figures S1 and S2 in the revised manuscript.

The relevant parts in the revised manuscript are addressed in Section 2:

"The GOBAI-O_2 data are the oxygen data on 1° × 1° horizontal grid with 58 vertical levels at the following depths: 2.5, 10, 30, 40, 50, 60, 70, 80, 90, 100, 110, 120, 130, 140, 150, 160, 170, 182.5, 200, 220, 240, 260, 280, 300, 320, 340, 360, 380, 400, 420, 440, 462.5, 500, 550, 600, 650, 700, 750, 800, 850, 900, 950, 1000, 1050, 1100, 1150, 1200, 1250, 1300, 1350, 1412.5, 1500, 1600, 1700, 1800, 1900 and 1975 m). High vertical resolution near the surface is essential for accurately capturing strong temperature, salinity, density, and oxygen gradients in the mixed layer [Kara et al., 2000]. In our analysis relating to the isopycnal surfaces, we interpolated the original GOBAI-O_2 data to 1-m vertical resolution using cubic spline interpolation and gridded them onto a 1° × 1° × 1 m grid, because interpolation makes us evaluate linear trends in potential temperature, salinity, and dissolved O_2 for each latitudinal band at 1° intervals in latitude and at 0.1σ_θ intervals (Figs. 4–7). To evaluate whether this interpolation procedure is appropriate or not, we also conducted sensitivity tests using multiple interpolation methods (linear, shape-preserving cubic (PCHIP)) and coarser vertical grids (2m and 5m). The results showed no clear differences among the three interpolation methods (Figures S1 (a, b) and S2 (a, b)). A 5-m grid fails to resolve densities lighter than 24.0σ_θ at some latitudes, but we confirmed that the main features of the fields are preserved across all tested resolutions. "

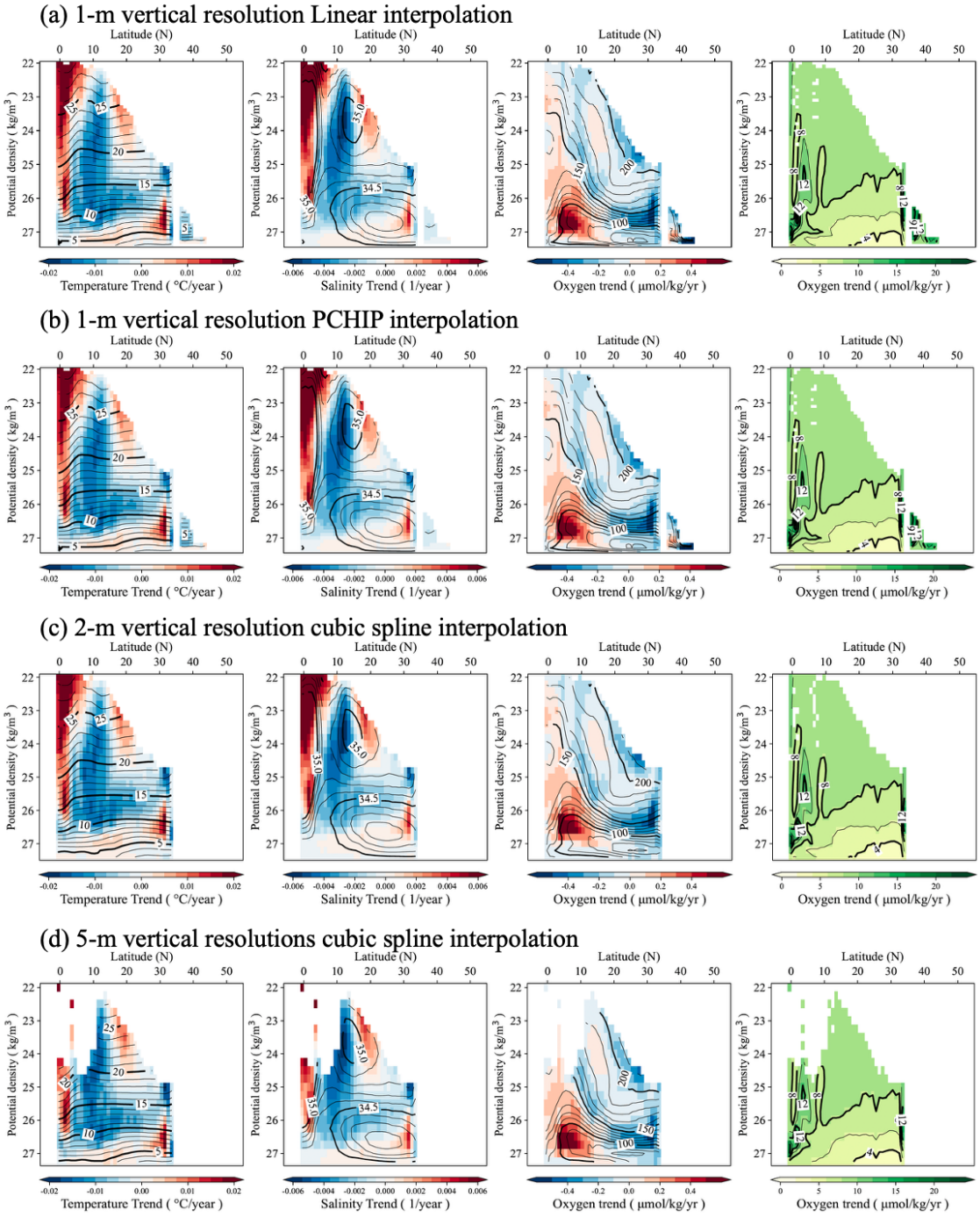

Figure S1 in the revised manuscript: Linear trends in potential temperature, salinity, dissolved O_2 and uncertainty on each isopycnal horizon in 137° E lines. The figures are the same as Figure 4, but using 1°× 1°× 1 m grid data generated data with linear (a) and RCHIP (b) interpolation methods. The 1°× 1°× 2 m and 1°× 1°× 5 m grid data generated data with cubic spline interpolation, respectively. Contour lines represent the mean values during the target observation periods, plotted at density intervals of 0.1σ_θ (a, b), 0.25σ_θ

(c, d) for each 1 deg, respectively.

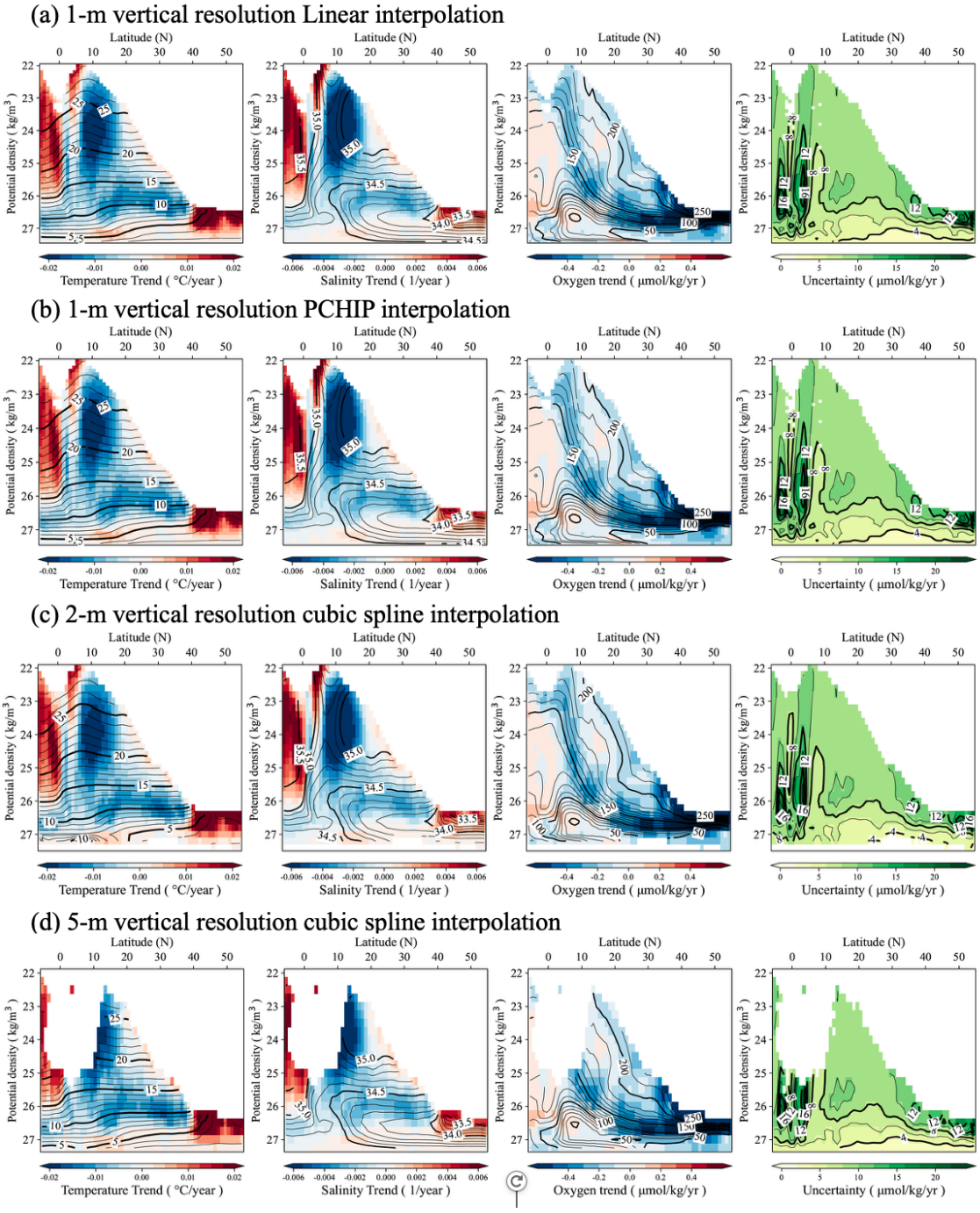

Figure S2 in the revised manuscript: Sams as Fig. S1, but in 165° E lines.

The decomposition of oxygen change following equation (2) is interesting but not easy to follow; a clearer derivation or schematic would help.

The derivations of equation (2) are written in detail by Sasano et al. (2015). We followed their deviation and added their derivations in Appendix A with schematic illustrations of Figure S5, in the revised manuscript.

The revised parts can be read in Appendix A and Figure S3 as follows:

Appendix: Essential concepts and derivations for Equation (2-3)

The essential concepts and derivation for equations (2) and (3) were originally proposed by Takatani et al. [2012] and described in detail by Sasano et al. [2015]. We follow their derivation here.

When the temperature at a depth z_A increases from θ_A to θ_A' as a consequence of ocean heat content increase, the density at that depth decreases from σ_A to σ_A'. For simplicity, the vertical profile of salinity is assumed to remain unchanged with time. As a result, the isopycnal surface of σ_A deepens from z_A to z_B (Figure S5). If surface freshening occurs simultaneously due to a net freshwater input, both the density decreases at z_A (from σ_A to σ_A') and the deepening of the isopycnal (from z_A to z_B) are enhanced. Because density is a function of temperature and salinity ($\sigma = f(\theta, S)$), the density of an isopycnal surface σ_A can be expressed as

$$\sigma_A = f(\theta_A, S_A) \qquad \text{(before warming)} \quad \text{(C1)}$$

$$= f(\theta_B', S_B). \qquad \text{(after warming)} \quad \text{(C2)}$$

Here, S_A and S_B denote salinity at depth z_A and z_B, respectively, and θ_B' represents the temperature at σ_A at z_B after warming. To satisfy (C1) and (C2), z_B is determined. In the region where salinity decreases with depth (e.g., above the salinity minimum layer of NPIW), $S_A > S_B$, and thus $\theta_A > \theta_B'$. This means that the potential temperature on an isopycnal surface effectively decreases as a result of warming, implying that biogeochemical properties on an isopycnal surface are also expected to change.

For a tracer X whose vertical profile with respect to depth does not change with time (e.g., salinity; see Figure S5(c)), the temporal change of X on potential density σ_A is attributed to the apparent change caused by the deepening of the isopycnal surface from z_A to z_B:

$$\frac{\partial X}{\partial t} = \left(\frac{\partial X}{\partial z} \cdot \frac{\partial z}{\partial t}\right) \qquad \text{(C3)}$$

Here, $\partial X/\partial t$ represents the temporal change of X observed on σ_A (gray arrows in Figure S5), z the depth at σ_A, $\partial X/\partial z$ the vertical gradient of X with respect to the depth (assumed to be time-invariant), and $\partial z/\partial t$ the rate of increase in the depth of density σ_A. $\partial X/\partial z \cdot \partial z/\partial t$ denotes the effect of deepening (illustrated as white arrows in Figure S5, corresponding to the difference between the filled square and filled circle).

Alternatively, for a variable Y whose vertical profile evolves with time and warming occurs simultaneously, the temporal change of Y at density σ_A can be expressed as the sum of two components: the temporal change associated with the deepening of the isopycnal surface from z_A to z_B and the net temporal change of Y, $(\partial Y/\partial t)_{net}$ between the time before and after warming:

$$\frac{\partial Y}{\partial t} = \left(\frac{\partial Y}{\partial z} \cdot \frac{\partial z}{\partial t}\right) + \left(\frac{\partial Y}{\partial t}\right)_{net} \qquad \text{(C4)}$$

To evaluate the net change $(\partial Y/\partial z)_{net}$ (illustrated by the black, blue, or pink arrows of a difference in symbols between filled square and open square in Figure S5), it is necessary to evaluate the contribution of the temporal change of Y due to the deepening of the isopycnal surface and to subtract it from the change of Y observed at density σ_A. For instance, the change of O_2^{sat} in Figure S5(f) is observed as a gray isopycnal surface (white arrow). Therefore, the net change (blue arrow) is obtained as a difference between the observed change and the deepening effect.

The dissolved oxygen concentration O_2 can be expressed as:

$$O_2 = O_2^{sat} - AOU \qquad \text{(C5)}$$

where O_2^{sat} is the oxygen saturation concentration (a function of temperature and salinity) and AOU is "apparent oxygen utilization". AOU represents the oxygen consumed by biological activity since subduction. However, these contributions are typically negligible because AOU ≈ 0 in surface waters.

According to (C4), the temporal change of O_2 at a given density for a fixed station is:

$$\frac{\partial O_2}{\partial t} = \left(\frac{\partial O_2}{\partial z} \cdot \frac{\partial z}{\partial t}\right) + \left(\frac{\partial O_2}{\partial t}\right)_{net}. \qquad \text{(C6)}$$

Similarly,

$$\frac{\partial O_2^{sat}}{\partial t} = \left(\frac{\partial O_2^{sat}}{\partial z} \cdot \frac{\partial z}{\partial t}\right) + \left(\frac{\partial O_2^{sat}}{\partial t}\right)_{net}, \quad \text{(C7)}$$

and

$$\frac{\partial AOU}{\partial t} = \left(\frac{\partial (AOU)}{\partial z} \cdot \frac{\partial z}{\partial t}\right) + \left(\frac{\partial (AOU)}{\partial t}\right)_{net}. \quad \text{(C8)}$$

The term $(\partial O_2^{sat}/\partial t)_{\text{net}}$ is directly related to a certain value with respect to warming as O_2^{sat} changes as a function of temperature. If AOU does not change with time, i.e., the change in O_2 concentration is attributed only to the change in O_2^{sat}, $(\partial (AOU)/\partial \text{t})_{net} = 0$ and $\partial (AOU)/\partial t$ follow equation (C3). On the other hand, if AOU varies with time, $\partial (AOU)/\partial t$ follows equation (C4) and $(\partial (AOU)/\partial \text{t})_{net} \neq 0$, as shown by dashed gray line in Figure S5(g).

Since O_2 is expressed as equation (C5), the net temporal change of O_2 on an isopycnal surface is given by:

$$\left(\frac{\partial O_2}{\partial t}\right)_{net} = \left(\frac{\partial O_2^{sat}}{\partial t}\right)_{net} - \left(\frac{\partial (AOU)}{\partial t}\right)_{net}. \quad \text{(C9)}$$

According to equations (C6) and (C9), the temporal change of O_2 on an isopycnal surface can be expressed:

$$\left(\frac{\partial O_2}{\partial t}\right) = \left(\frac{\partial O_2}{\partial z} \cdot \frac{\partial z}{\partial t}\right) + \left(\frac{\partial O_2^{sat}}{\partial t}\right)_{net} - \left(\frac{\partial (AOU)}{\partial t}\right)_{net}, \quad \text{(C10)}$$

as described in equation (1) in the main text. Each term in equation (C10) corresponds to an arrow in Figure S5(e): From left to right, these are represented by the gray arrow, white, blue and pink arrows, respectively. The blue arrow is identical to Figure S5(f), while pink arrow corresponds to Figure S5(g), but with its direction reversed. Finally, substituting equations (C7) and (C8) into (C10) yields (C11) (corresponding to equation (2) in the main text):

$$\frac{\partial O_2}{\partial t} = \left(\frac{\partial O_2}{\partial z}\frac{\partial z}{\partial t}\right) + \left(\frac{\partial O_2^{sat}}{\partial t} - \frac{\partial O_2^{sat}}{\partial z}\frac{\partial z}{\partial t}\right) - \left(\frac{\partial (AOU)}{\partial t} - \frac{\partial (AOU)}{\partial z}\frac{\partial z}{\partial t}\right). \quad \text{(C11)}$$

(i) (ii). (iii). (iv) (v) (vi)

Note: The signs in Eq. 3(v) and (vi) are reversed from those in Equations C11(v) and (vi) for convenience.

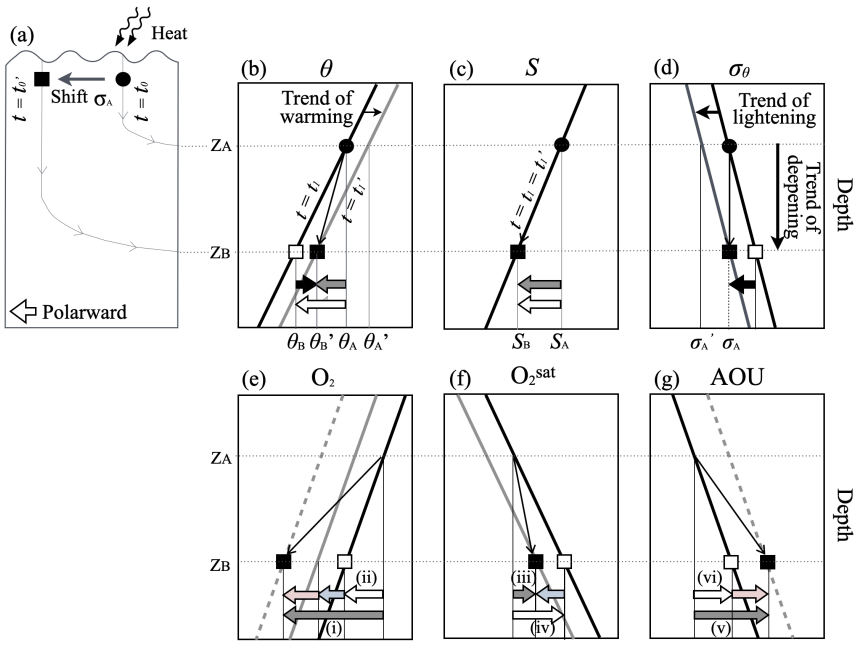

Figure S5 in the revised manuscript: Schematic illustration of the temporal evolution of parameters on a typical (a) isopycnal horizon above a salinity minimum layer: (b) potential temperature (θ), (c) salinity (S), (d) potential density (σ_θ), (e) dissolved oxygen (O_2), (f) oxygen saturation (O_2^{sat}), (g) apparent oxygen utilization (AOU). Thick black (gray) lines indicate the vertical profiles before (after) warming at a time t_1 (t_1'). Dashed gray lines represent profiles after warming, accompanied by a concurrent increase in AOU. Dotted lines in panel (d) denote the isopycnal horizons considered here. Closed cycles and squares denote water parcels observed at a depth Z_A and Z_B, respectively, at times between time t_0 and t_1. The time refers to the period between each parcel submergence. Gray arrows indicate the observed temporal changes along a density horizon ($\partial X/\partial t$), while white arrows denote apparent changes by the vertical deepening effect ($\partial X/\partial z \cdot \partial z/\partial t$). Large blue and pink arrows in panels (e-g) represent net change (= gray arrow - white arrow). The textured arrows with identical patterns indicate identical processes. Arrows labeled with Roman numerals correspond to the respective terms in equation (2). These schematics are after Sasano et al. (2015).

Some of the proposed mechanisms, for example the role of NEC/NECC migration, are plausible but speculative unless supported by independent evidence such as altimetry or reanalyses. Finally, the exclusive focus on linear trends risks obscuring the role of low-frequency climate variability such as the PDO or NPGO.

Thank you for your suggestion. After receiving your comments, we revisited previous studies on ocean variability in the western equatorial Pacific, including Qiu and Chen (2012), and gained further insights from Chen et al. (2016): Variabilities in the North Equatorial Countercurrent (NECC) in the western Pacific are primarily governed by interannual and decadal timescale fluctuations.

Guided by Chen et al. (2016), we analyzed the OFES dataset used in their study and found a new finding for the increase of the oxygen linear trends from 2004 to 2023 in the western equatorial region, which can be explained by the variability associated with the second EOF mode of the NECC, as highlighted in their work. Based on this new analysis, we have revised the relevant sections of the manuscript accordingly (Section 3.3.2).

The revised part in Section 3.3.2 now reads:

"The increases in dissolved O_2 are particularly prominent in the western tropical area at the density range of 26.8–27.2 σ_θ (Fig. 3c and g; Fig. 4c and g; Fig. 5c, f, and i). This area overlaps with the OML [Reid, 1997]. A similar tendency has also been reported by Sasano et al. [2015] and Takatani et al. [2012]. In this area, the physical variability of the North Equatorial Counter Current (NECC) is likely relevant. Following Chen et al. [2016], the NECC exhibits two distinct modes of variability –interannual and interdecadal– based on the outputs of a multidecadal (1960–2014) ocean general circulation model for the Earth Simulator (OFES). The first mode fluctuates on an interannual timescale, strengthening with a southward migration. The second mode occurs on an interdecadal timescale and is characterized by a progressive weakening in strength, poleward migration, and broadening in width. Their analysis further suggested that, for the second mode, a decrease in wind-curl intensity near the equator was responsible for the weakening, poleward migration, and widening of the current.

The time-varying signals in the western tropical Pacific in the OFES data are validated by Chen et al. [2016]. We then examined the OFES data (1950–2023), as well, for poleward, eastward velocities, as well as potential temperature and salinity here. The potential temperature anomalies in the OFES data (Fig. 9c, g) indicate that positive anomalies in 0°–5 °N occur above 250 m depth, whereas negative anomalies appear along the potential density along 26.0σ_θ between 5°–20°N. A similar pattern is also shown in the GOBAI-O_2 data (Fig. 3a). There is a discrepancy: Negative trends in salinity along

26.0σ_θ are captured in GOBAI-O_2 data (Fig. 3 b), whereas positive trends in salinity along 26.0σ_θ are detected in the OFES model (Figs. 9b, f). This discrepancy is likely due to the higher salinity present between 200–600 m depth in 0–7°N in OFES, which differs from GOBAI-O_2 data (Fig. 10b, d).

Anomalies of the poleward and eastward velocities from 1950 to 2023 and from 2024 to 2023 (Fig. 9a–b, e–f) indicate that poleward velocities increase around 5°N above 200m depth, while eastward velocities decrease in 0–4°N and increase in 5–7°N. The main axis of eastward velocity certainly shifts poleward in 137 °E lines (Fig. 11a), consistent with changes in the second mode variablity of the NECC detected by Chen et al. [2016]. The maximum of the poleward velocity of the NECC is also shifted northward from 1964 to 2023 continuously (Fig. 11b). The broadening of NECC width was not apparent in this analysis, differing from Chen et al. [2016]. This could be because we analyzed the original data rather than isolating the second EOF mode of the velocities. Examination of the wind-curl intensity in the equatorial region from 1950 to 2023 confirmed that the decreases in wind-curl intensity along the 0°–10°N band and the poleward broadening of the negative wind stress curl have persisted to 2023 (Fig. 12).

The westward penetration of the OML is slow, occurring between two eastward-extending tongues of high O_2 water originating from the western boundary around the equator area [Reid, 1997]. The O_2 increase at the density range of 26.8–27.2 σ_θ (Fig. 3c, g and Fig. 4c, g) could therefore be explained from weakening and north-poleward shifts of the second mode of the NECC with interdecadal variability. The O_2 increase (Fig. 1o-u) follows with such physical backgrounds, penetrating larger dissolved O_2 from westward. The depth of the isopycnal surface becomes shallower along the equator during the observational period in the boundary between the subtropical gyre and the tropical region, meaning the boundary shifts to the north along 137°E line.”

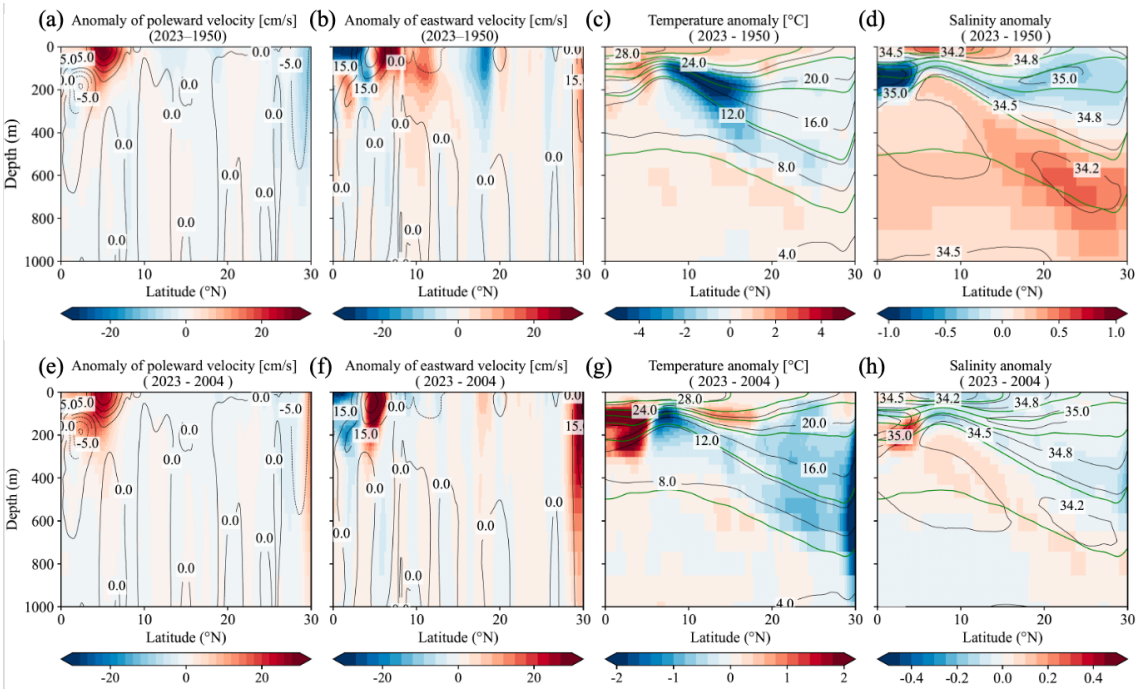

Figure 9 in the revised manuscript: Anomaly of poleward and eastward velocity, potential temperature, and salinity in the OFES model outputs from 1950 to 2023 (a–d) and from 2004 to 2023 (e–h), respectively, in the 137°E line. Contours of averaged values of poleward and eastward velocity, potential temperature, and salinity during the target period are also shown in each figure. Green contour lines in (c–d, g–h) indicate the average potential density of 22, 23, 24, 25, 26 and 27σ_θ, during the target periods.

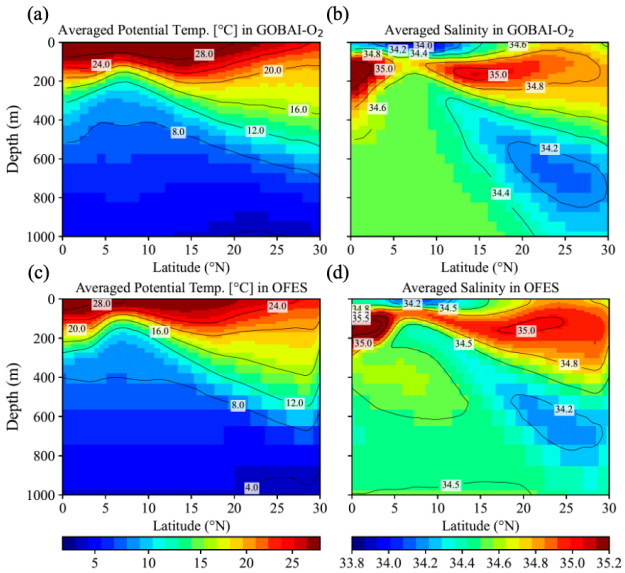

Figure 10 in the revised manuscript: Averaged Potential Temperature (a, c) and salinity (b, d) in GOBAI-O_2 from 2004 to 2023 and OFES data from 1950 to 2023, respectively,

in the 137°E line.

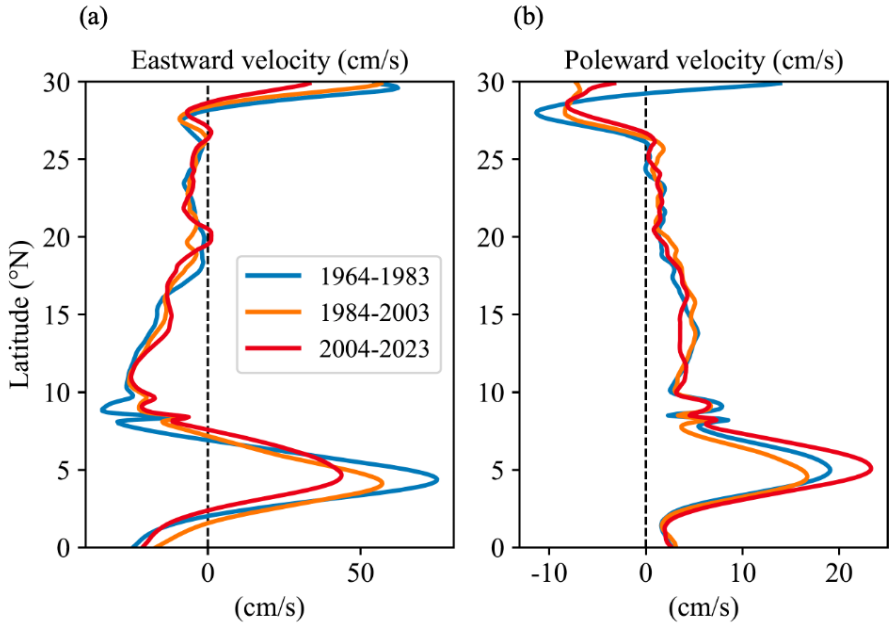

Figure 11 in the revised manuscript: Latitudinal distribution of averaged eastward (a) and poleward velocity (b) in the OFES data from 1964 to 1983, from 1984 to 2003, and from 2004 to 2023, respectively, in the 137°E line.

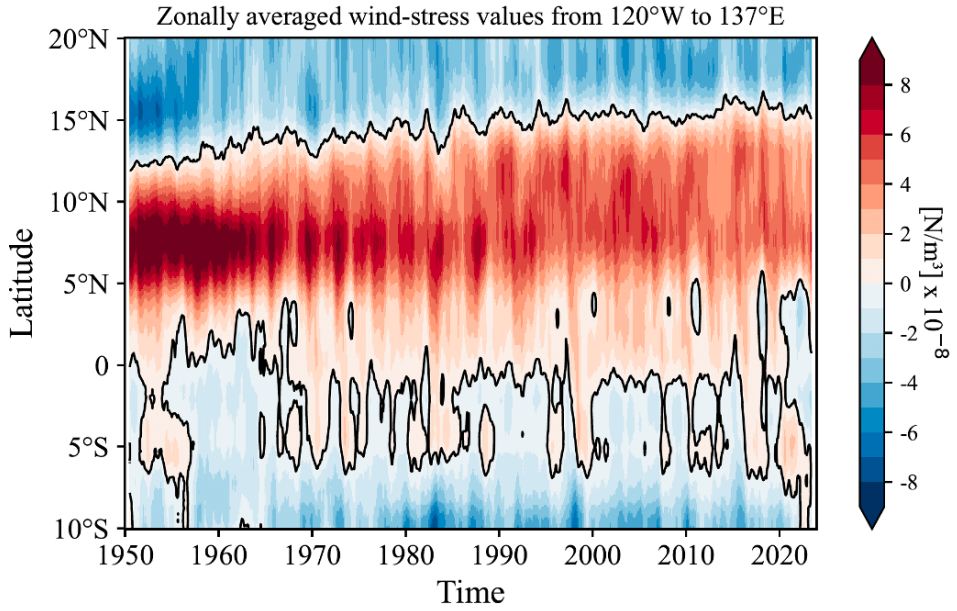

Figure 12 in the revised manuscript: NCEP-NCAR wind-stress curl values zonally averaged from 120°W to 137°E from 1950 to 2023. A 13-month running-mean filter

has been applied in time.

The language and presentation require significant improvement. Numerous grammatical errors hinder readability, and several figures, especially the large multi-panel maps, are overly dense. A careful edit and improved figure design would considerably enhance clarity.

We carefully checked for grammatical errors. Should you happen to find any grammatical errors, I would appreciate it if you could point them out to me.

In conclusion, the dataset is of great interest and the paper has merit, but substantial revision is needed. The authors should better situate their findings relative to previous work, integrate uncertainties and known biases into their interpretation, clarify methodological choices, and moderate or substantiate their physical explanations. With these improvements, the manuscript could become a valuable contribution to our understanding of oxygen variability in the North Pacific.

Thank you for your valuable time in reviewing this manuscript. I hope you find the revised version satisfactory. However, if it still falls short, we would appreciate any additional suggestions you may have.